

3-D magnetic configurations supporting prominences

III. Evolution of fine structures observed in a filament channel

G. Aulanier¹, P. Démoulin¹, N. Mein¹, L. van Driel-Gesztelyi^{1,2}, P. Mein¹, and B. Schmieder^{1,3}

¹ Observatoire de Paris, section Meudon, DASOP/LPSH, F-92195 Meudon Principal Cedex, France

² Konkoly Observatory, Budapest, Pf. 67, H-1525 Hungary

³ University of Oslo, P.O. Box 1029, Blindern, N-0315 Oslo, Norway

Received 22 June 1998 / Accepted 29 October 1998

Abstract. On September 25th 1996, a quiescent filament located near the center disc (S2, E5) was observed on the German VTT (Tenerife) with the MSDP instrument, in the H α line center and wings. SOHO/MDI line-of-sight magnetograms were co-aligned with the MSDP images, showing the position and evolution of the lateral feet of the filament in the vicinity of the parasitic magnetic polarities observed in the filament channel.

Using the assumptions developed in the previous papers of this series related to the reconstruction of the 3-D magnetic configuration of filaments, we perform “linear magnetohydrostatic” extrapolations (taking into account the effects of plasma pressure and gravity) on the SOHO/MDI magnetograms. The main hypothesis is the presence of a twisted flux-tube located above the photospheric inversion line.

Assuming that the parameters of the model do not need to be significantly modified during the evolution of the configuration for a duration of 1 day, we have shown that the 3-D distribution of dipped field lines is well correlated with H α dark absorbing features in the filament channel: the filament itself, its lateral feet and some of the surrounding dark fibrils. In this way we confirm what was suggested in our earlier papers, i.e. that the feet are composed of the dipped portions of some field lines, which form a continuous pattern from the corona to the photosphere. We propose the same explanation for the magnetic configuration of some of the dark H α fibrils in the channel. We show that the plasma effects are not responsible for the existence of most of the magnetic dips, however their inclusion helps to get a better correspondence between the model and the observations. We find that the average H α Doppler velocities associated with the filament and with the chromospheric fibrils is of the order of a few hundred m s⁻¹ (though it can go locally up to 3 km s⁻¹ in the filament). These upward velocities are consistent with a quasi-static evolution of the magnetic configuration and with the support of dense plasma in magnetic dips.

Key words: Sun: prominences – Sun: magnetic fields – Sun: filaments – Sun: chromosphere – Magnetohydrodynamics (MHD)

1. Introduction

The magnetic field plays a key role in all the processes involved in the corona as in prominences because the plasma beta is low (in the range of 10⁻³ to 10⁻¹). It channels both the plasma motions and the thermal conduction. It provides support against gravity of the prominence plasma one hundred times denser than the coronal plasma. This primary role is not always recognized at its right level because the majority of observations are focused on the plasma, though Hanle effect measurements of the magnetic field inside prominences have been obtained as well (see Bommier & Leroy, 1998 and references therein). Furthermore, the importance of the magnetic field is less evident in prominences than in other phenomena since usually the prominence plasma does not directly visualize field lines as it does in arch-filament systems, surges and coronal loops.

On one hand 3-D models of the magnetic configurations are difficult to build, since the configurations are strongly non-potential and the electric current distribution is unknown. On the other hand it is challenging to understand the presence of filaments in the corona with their characteristic feet that reach the photosphere (see Démoulin, 1998). This problem also has a much larger impact on solar physics in general: it brings valuable informations on the global solar magnetic field with direct implications on dynamo theories (e.g. Berger 1998) and on the solar activity (like the launch of CMEs, see e.g. Low 1996). Consequently, knowing the typical magnetic configurations for filaments leads to consider them as local tracers of the coronal magnetic configuration. Filament observations combined with their associated longitudinal photospheric magnetic fields bring important constraints on the determination of the associated 3-D magnetic configuration.

In previous papers (Aulanier & Démoulin 1999, hereafter Paper I, and Aulanier et al., 1998, hereafter Paper II), we have shown that a twisted flux-tube is the most probable magnetic configuration supporting prominences. The model interprets many observations in a natural way (in particular the magnetic measurements in prominences and the chirality properties). Prominence feet appear as a direct consequence of the parasitic polarities present in the filament channel. In particular, we showed that the prominence lateral feet appear naturally,

Send offprint requests to: G. Aulanier

Correspondence to: aulanier@mesopa.obspm.fr

above secondary photospheric magnetic inversion lines and we described the morphological change of feet as the parasitic polarities evolve. We also related the topological properties of the deduced magnetic configuration (i.e. the separatrices) to chromospheric brightenings.

The purpose of this paper is to extend the previous results of Paper II. In this paper, a detailed consideration of observations give more precise constraints to the model, which is improved here. The set of observations related to the studied filament channel ($H\alpha$ data and photospheric magnetograms) is described in Sect. 2. Then in Sect. 3, we explain the method used to compute the magnetic field in the corona; it was developed by Low (1992) and now applied to observations. The present method differs from Paper II where we used magnetic charges to describe the magnetogram while here we use directly the magnetograms for the field computation. Moreover, the present model takes into account the effects of gravity and of plasma pressure, while in Paper II the magnetic field was modeled in the force-free approximation. We then describe in Sec. 4 the results of the reconstruction of the 3-D magnetic field constrained by one of the magnetograms, and compare the distribution of magnetic dipoles in 3-D with the morphology of the $H\alpha$ filament and its surrounding fibrils. In Sect. 5 we investigate the importance of pressure and gravity on the computed magnetic configuration. In Sect. 6 we follow the evolution of the main body of the filament, as well as one of its lateral feet and one of its surrounding group of dark fibrils, assuming a quasi-static evolution of the magnetic field. We confirm what was only suggested in Paper II, i.e. that the evolution of the $H\alpha$ dark fine structures in the filament channel is driven by the photospheric evolution of parasitic polarities. The observed vertical flow pattern obtained from $H\alpha$ Dopplershifts is then described in Sect. 7. It shows that the quasi-static assumption is justified by the observations. The Dopplershifts are then discussed in the context of the computed magnetic configuration. We summarize the results in Sect. 8, and we put them in a more general context.

2. Observations

On September 1996, a quiescent filament channel was observed in the decaying remnant of AR 7986. The observations were obtained during a coordinated campaign between space instruments (SOHO and Yohkoh) and ground-based instruments (the German VTT and GCT at the Teide Observatory, Tenerife, and the SVST at La Palma), in the context of the Joint Observing Program JOP 17 concerning the study of the “Dynamics of Solar Active Region”. In this paper we only use $H\alpha$ observations obtained with the MSDP instrument mounted on the VTT, as well as SOHO/MDI line-of-sight magnetograms taken on September 25th.

2.1. MSDP observations in $H\alpha$

The details of MSDP data reduction is described in Mein (1991). Nine images of the same solar area were recorded simultaneously in nine wavelengths of the $H\alpha$ profile on a 1024×1024 CCD camera. By using 200 successive steps across the solar

Table 1. List of the SOHO/MDI magnetograms and MSDP $H\alpha$ data used in this paper (observed on September 25th 1996). It must be noted that the times of $H\alpha$ data and MDI magnetograms correspond to the beginning of the scans (of which duration is a few minutes).

Magnetogram		$H\alpha$ image
Time UT	Threshold Gauss	Time UT
07:40	10	08:43
12:53	3	12:14
15:59	10	15:57
17:35	10	17:04

disk, we scanned two strips of 170×600 arcsec² every 34 min. The elementary fields of view are overlapping. They are joined by 2-D cross-correlation calculations. The pixel size is $0.43''$ for the recording, and $0.25''$ for the output maps. The MSDP also observed simultaneously with $H\alpha$ the selected strips in the y line (Ca II, 8542 Å), of which dotted brightenings are relevant of the underlying magnetic network.

The $H\alpha$ profile is restored at each point of the field. A special care is taken to correct the scattered light in the spectrograph. Dopplershifts and intensity fluctuations are derived at different distances from line center. The $H\alpha$ images of the filament channel presented in this paper are computed at ± 0.25 Å from line center.

2.2. SOHO/MDI magnetograms

MDI is one of twelve experiments onboard the SOHO spacecraft, which was launched on December 2, 1995. The Solar Oscillations Investigation (SOI) uses the Michelson Doppler Imager (MDI) instrument to probe the interior of the Sun by measuring the photospheric manifestation of solar oscillations (Scherrer et al., 1995). The instrument images the Sun on a 1024×1024 CCD camera through a series of increasingly narrow filters. The final elements, a pair of tunable Michelson interferometers, enable MDI to record filtergrams with a FWHM bandwidth of 100 mÅ. Several times each day polarizers are inserted to determine the line-of-sight magnetic field. In this paper we are using magnetograms of the full-disc mode with a 96-minute cadence, with a pixel size of $2''$. Some maps are made using a five-minute average of the polarization signal, while others are merely “snapshots”.

The noise in the magnetograms originates from two main components: photon shot noise and leakage from the Doppler signal. Single magnetograms are limited by the shot noise to about ± 10 Gauss and five-minute average maps to about ± 3 Gauss. That is because over the five-minute interval most p-modes execute almost one complete cycle, so the P-mode leakage is smaller. There is some noise at about the 2–3 Gauss level from granulation as well (DeForest, private communication).

In Table 1 we list the magnetograms available during the MSDP observing hours on September 25th 1996. Unfortunately, during the morning hours, when the seeing is the best on Tener-

ife, two magnetograms were lost presumably due to telemetry problems. We match the magnetograms with the MSDP image taken at the closest in time.

2.3. Co-alignment of the MDI and MSDP data

Since the MSDP instrument has a partial field of view and no pointing information, the co-alignment of the MSDP and MDI images is not trivial, thus we need to use additional observations, such as full-disc $H\alpha$ images and y line (Ca II, 8542 Å) MSDP images to place the partial MSDP $H\alpha$ image on the solar disc. We rotated a full disc Meudon $H\alpha$ spectroheliogram taken at 14:35 UT to the times of each MDI magnetograms and co-aligned the full-disc images. Then we co-aligned the full disc and partial field $H\alpha$ observations and “fine-tuned” the co-alignment matching relevant network brightenings observed on CaII MSDP images (taken coincidentally and co-spatially with the $H\alpha$ images, see Sect. 2.1) and magnetic polarities from the MDI magnetograms. In order to do so, we performed feature-tracking techniques in a large field of view (about 300×600 arcsec²). We estimate that the mis-alignment is not larger than 4'' (two MDI pixels).

We then located the observed straight inversion line using a large field of view (about 300×600 arcsec²), and for viewing reasons we finally rotated the co-aligned MDI magnetograms and MSDP images to place the inversion line vertically and at the center of the considered fields of view (see Fig. 1d). Thus, in all the figures of this paper, the true North is 72° to the left from up.

3. Reconstruction of the magnetic field in the filament channel

The aim of this section is to describe the model that we use for the reconstruction of the 3-D magnetic configurations of the observed filament channels. We use a magnetohydrostatic extrapolation method developed by Low (1992), which takes into account the effects of pressure and gravity on the magnetic field. Following the approach of Paper II, the observed inhomogeneous bipolar photospheric field component is replaced by a regular bipolar background field which constrains the presence of a twisted flux-tube.

3.1. Linear magnetohydrostatic equations

The equations governing magnetohydrostatic equilibrium are given by:

$$\frac{1}{\mu_0} (\nabla \times \mathbf{B}) \times \mathbf{B} - \nabla p + \rho \mathbf{g} = 0, \quad (1)$$

$$\nabla \cdot \mathbf{B} = 0. \quad (2)$$

Let's use a cartesian system of coordinates, where z refers to the height and (x, y) to planes parallel to the photosphere. Low (1991) has solved these equations by defining the current density ($\mathbf{j} = \nabla \times \mathbf{B} / \mu_0$) of Eq. (1) with Euler potentials. For any given function of the altitude $F(z)$, and keeping α constant as in the

linear force-free field (*lfff*), the linear magnetohydrostatic (*lmhs*) equations can be re-written as:

$$\nabla \times \mathbf{B} = \alpha \mathbf{B} + F(z) \nabla B_z \times \mathbf{u}_z, \quad (3)$$

where \mathbf{u}_z is the normalized vertical vector. From Eqs. (1) and (3), the plasma pressure and density can be expressed as follows:

$$p = p_0(z) - \delta p = p_0(z) - F(z) \frac{B_z^2}{2\mu_0}, \quad (4)$$

$$\rho = \rho_0(z) - \delta \rho = -\frac{1}{g} \frac{dp_0}{dz} + \frac{1}{\mu_0 g} \left[\frac{1}{2} \frac{dF}{dz} B_z^2 + F(\mathbf{B} \cdot \nabla) B_z \right] \quad (5)$$

where $p_0(z)$ is a function which is independent of the magnetic field, and which only varies with z . This defines a background pressure (and density). Only the depletions δp and $\delta \rho$ depend on the magnetic configuration. We choose $F(z)$ as a decreasing exponential with height, as Low (1992) did in order to compute the general properties of *lmhs* solutions:

$$F(z) = a \exp(-z/H), \quad (6)$$

where a and H are the plasma parameters.

3.2. Physical interpretation of the plasma parameters

The influence of the plasma on the magnetic field is described by $F(z)$ in Eq. (3). Its effect is to create currents in the (x, y) planes, parallel to the photosphere. In Eq. (6), a is the measure of the intensity of these currents at $z = 0$, where it is also the ratio between the pressure depletion δp and the magnetic pressure $B_z^2/2\mu_0$ (Eq. [4]).

Low (1992) has used values of a up to 4, leading to the creation of low-lying twisted configurations. This was due to the change of sign of B_z with low height. However this oscillating behavior of the solutions is unlikely to be physical. Aulanier et al. (1998b) have discussed the maximum value for a below which none of the \mathbf{B} harmonics oscillate due to the plasma effects. This value has been estimated to $a(\max) = 1$.

The vertical extension of the plasma effects is given by the scale-height H . Low (1992) explained in details how H can be in some cases equal or close to an isothermal pressure scale-height.

From Eq. (4), it is clear that the pressure depletion is larger as the magnetic field is more vertical. This is consistent with measurements of the pressure above strong fields, such as sunspots.

The properties of the density depletion are more complex, due to its expression (see Eq. [5]). Note that the last term is related to the curvature of the magnetic field, and that the density is higher in the presence of magnetic dips than in the case of arcades. This is consistent with finding dense plasma in magnetic dips, such as in filaments or dark fibrils (see Paper I and II). More details about the behavior of the pressure and density can be found in Low (1992) and Aulanier et al. (1998b).

It is noteworthy that the horizontal currents induced by the plasma have a component along the magnetic field when it is not vertical, so that the current density \mathbf{j} parallel to the field is

no longer equal to $\alpha \mathbf{B}$. As a consequence, a slight non-linearity in the current distribution versus the magnetic field is brought by the plasma (see Low, 1992). Though this method still differs from the non-linear magnetohydrostatics (*nlmhs*) where $\alpha \neq$ constant, thus we name the method as “linear” magnetohydrostatics (*lmhs*).

3.3. Extrapolation method

From Eq. (3), $\mathbf{B}(x, y, z)$ can be expressed as a series of *lmhs* harmonics. Low (1992) has shown that the horizontal Fourier transformation η_z of the vertical magnetic field component B_z is in the form of Bessel functions:

$$\eta_z(n_x; n_y) = \tilde{B}(n_x; n_y) J_s \left[q \exp \left(- \frac{z}{H} \right) \right], \quad (7)$$

where $q = 2KH\sqrt{a}$ and $s = 2H\sqrt{K^2 - \alpha^2}$. $K^2 = k_x^2 + k_y^2$, where k_x and k_y are the wavenumbers with respect to x and y , being equal to $k_x = 2n_x\pi/L_x$ and $k_y = 2n_y\pi/L_y$. (L_x, L_y) are the periodicities, and (n_x, n_y) the orders of the considered harmonics, in the (x, y) directions respectively. $\tilde{B}(n_x; n_y)$ is the amplitude of the harmonic related the wavenumbers (k_x, k_y) .

For the study of any particular active region, the boundary conditions $B_z(x, y, z = 0)$ (which is equal to the observed longitudinal component when the studied region is at the disc center) need to be imposed from an observed magnetogram. A fast Fourier transformation firstly permits to decompose these boundary conditions in the form of *lmhs* harmonics (see Eq. [7]), and secondly to calculate $\mathbf{B}(x, y, z)$ at any z . Consequently it is noteworthy that the *lmhs* method requires periodic boundary conditions. More details on the extrapolation method and on the transformation of coordinates can be found in Démoulin et al. (1997) and Aulanier et al. (1998b).

3.4. Imposing a twisted flux-tube

A direct extrapolation of the magnetic field of the SOHO/MDI magnetograms (shown in Fig. 1d) in the *lfff* assumption does not provide the existence of a twisted flux-tube. This point has already been discussed in Paper II. We have realized in the present study that direct *lmhs* extrapolations also failed to create twisted flux-tubes, imposing the physical constraints that the field strength decreases at large heights and that *lmhs* harmonics are not oscillating with height.

Following the justifications listed in Appendix A, we impose a background field which, when a high magnetic shear is imposed (see Paper I), constrains the presence of a twisted flux-tube. The OX flux-tube that was used in Paper II is kept in this study. This “OX” terminology has been introduced in Paper I, where “O” refers to an O-point at the center of the flux-tube, and “X” to an X-point at its bottom, just like the model proposed by Kuperus & Raadu (1974). The difference is that it satisfies the *lmhs* equations (Eq. [3]). The flux-tube field is expressed by harmonics of which amplitudes are:

$$\tilde{B}(1; 0) = f; \quad \tilde{B}(2; 0) = -0.83 f; \quad \tilde{B}(3; 0) = 0.71 f, \quad (8)$$

where the parameter f is a multiplicative factor which has to be chosen in order to define the strength of the imposed background

field with respect to the strength of the observed fields. The value of f is discussed in Sect. 4.1. The critical value of the normalized value of α above which an OX flux tube appears in *lfff* with the parameters listed in Eq. (8) is $\alpha \simeq 0.988$.

3.5. Reconstruction of the magnetogram

The main bipolar component of the vertical field observed with SOHO/MDI has a mean width of 125 Mm (see Fig. 1d). We select such restrictive extension ($L_x = 125$ Mm) since the *lmhs*, like the *lfff*, extrapolation is not able to describe areas having localized strong magnetic shears (as in filament channels) which are embedded in a region having a weaker shear (as in the large scale coronal loops overlaying the filament), which is the typical distribution of the magnetic shear in the environment of filaments (as proposed by Antiochos et al., 1994 and Schmieder et al., 1996). Then the background field (shown in Fig. 1f) can be combined with the observed field (shown in Fig. 1d) as follows:

In a first step, the inhomogeneous bipolar component of the SOHO/MDI magnetogram is cut, so that only the observed magnetic field that lies between $x = \pm 37$ Mm on each side of the inversion line (situated at $x = 0$) is kept. By this way only the polarities in the filament channel are taken into account. In a second step, the theoretical background field (which ensures the presence of a twisted flux-tube with a large shear) is added to this cut magnetogram. Consequently, the observed dispersed bipolar component in the original magnetogram is replaced by a more regular one which is well aligned with the inversion line. Furthermore, a weak modulation of the field is brought by the theoretical background field in the region where $x = \pm 37$ Mm. But this only slightly modifies the polarities in the filament channel.

The constructed magnetogram is represented in Fig. 1e. It is noteworthy that the periodic boundary conditions required by the *lmhs* method lead to the fact that the positive flux on the right of Fig. 1e is only weakly connected to the negative flux on the left, although this still allows the presence of the twisted flux tube and some overlaying arcades.

At this point, *lmhs* or *lfff* extrapolations can be made using this constructed magnetogram (Fig. 1e) as boundary conditions.

4. The 3-D *lmhs* configuration for the filament channel at 12:14 UT

In this section we compare the reconstructed 3-D magnetic configuration with features in the filament channel observed on September 25th 1996 at 12:14 UT (see Sect. 2). We show that for realistic values of the parameters of the model, the morphology of the body of the filament, as well as the location and shape of its lateral feet and some fine structures in the filament channel, are well correlated with the location of the dipped portion of upwards curved field lines.

4.1. The parameters of the model: a , H , α , D and f

The first parameters that have to be fixed are the so-called “plasma parameters”, namely a and H , which are defined in

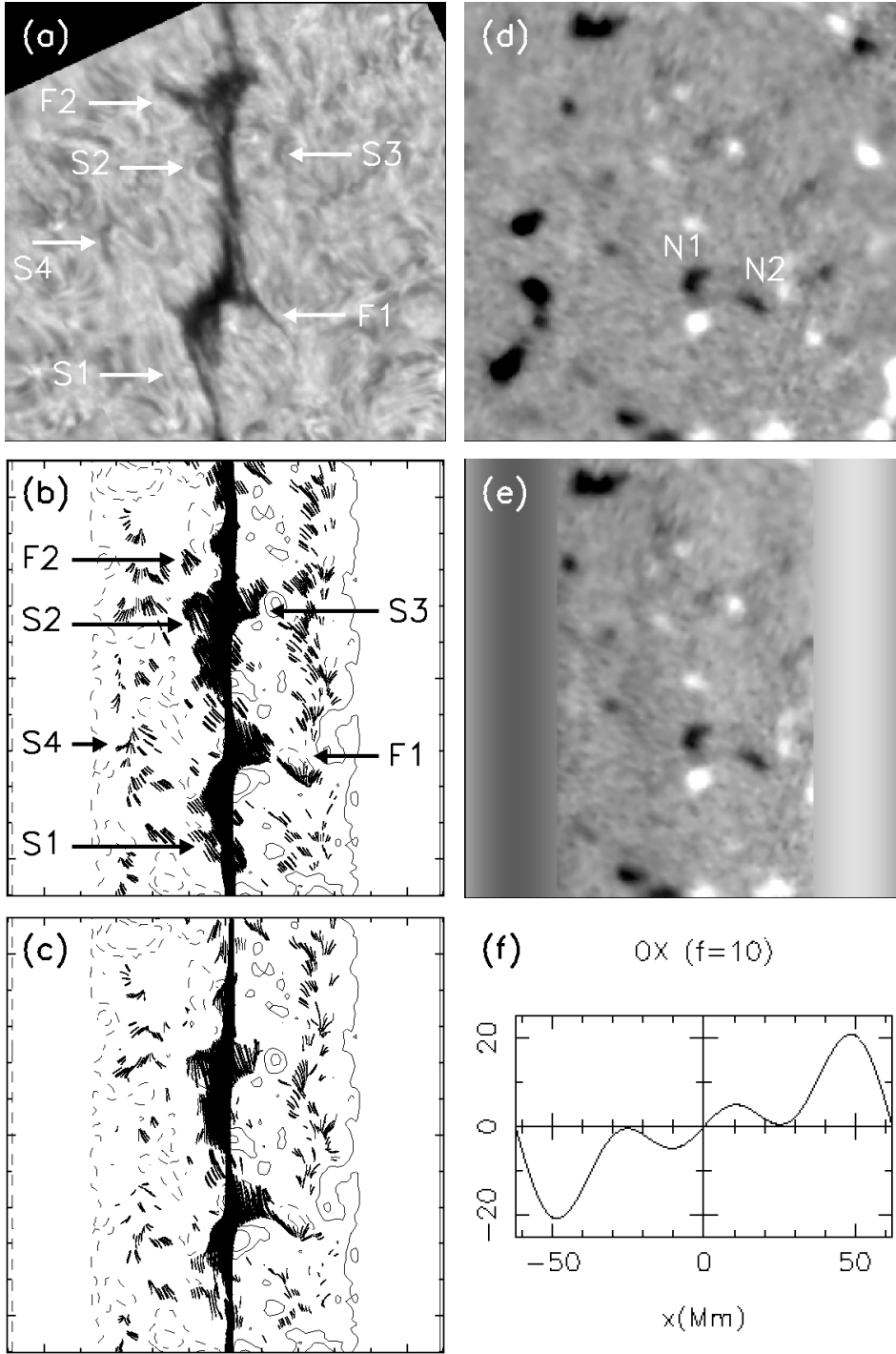


Fig. 1. **a** is the filament channel observed in the $H\alpha$ line-center with the MSDP on the German VTT (Tenerife), on September 25th 1996 at 12:14 UT. **d** shows the corresponding co-aligned SOHO/MDI line-of-sight magnetogram obtained at 12:53 UT. **f** shows a plot of the vertical component of the imposed background magnetic field that creates the twisted flux-tube. **e** shows the modified magnetogram for $f = 10$, which is a combination of the observed magnetogram and of the background field (see Sect. 3.5 for details). On **b** the dark lines correspond to the 3-D distribution of dipped field lines computed from a linear magnetohydrostatic (*lmhs*) extrapolation from the modified magnetogram obtained at 12:53 UT, using the *lmhs* parameters given in Table 2. The dips are represented up to a depth of $D = 300$ km. The dips are computed at regular intervals: $\Delta x = 0.75$ Mm, $\Delta y = 1.5$ Mm and $\Delta z = 2$ Mm. The thin full (resp. dashed) lines correspond to isocontours of the photospheric vertical magnetic field of 8 and 24 G (resp. negative values). **c** is the same as **b** except that the dips are computed from a linear force-free field (*lfff*) extrapolation (i.e. using $a = 0$ in Table 2). All the fields of views are $125\text{ Mm} \times 125\text{ Mm}$, or $172'' \times 172''$.

Table 2. Values of the parameters used for linear magnetohydrostatic (*lmhs*) extrapolations: $\tilde{B}(n_x; 0)$ are the amplitudes of the harmonics which define the twisted flux-tube, L_x and L_y are the size of the computational box and define the periodicity for *lmhs* extrapolations, α is the shear parameter, D is the depth of which the dipped field lines are presented, a is related to the strength of the plasma effects and H is the scale height on which the plasma effects are present.

$\tilde{B}(1; 0)$ (G)	$\tilde{B}(2; 0)$ (G)	$\tilde{B}(3; 0)$ (G)	f	L_x (Mm)	L_y (Mm)	α (Mm^{-1})	D (km)	a	H (Mm)
f	$-0.83 f$	$0.71 f$	10	125	125	0.05	300	1	10

Sect. 3.1. We have given the value of $a(\max) = 1$ in Sect. 3.2. Consequently, since we want to investigate the maximal effects of pressure and gravity on the reconstructed magnetic field configurations, we choose to use $a = 1$ for all the following extrapolations.

We choose a typical value of $H = 10$ Mm in order to have significant plasma effects in the prominence body, as typical prominences are known to be up to a few tens of Mm high. Moreover, filaments are composed of over-dense plasma with respect to the surrounding corona. Consequently it is worth to keep in mind that the plasma effects will be over-estimated in the corona surrounding the modeled filament.

An important parameter that needs to be fixed is the shear parameter α . Using the results of Paper II where a preliminary successful comparison has been made with a value of $\alpha = 0.05 \text{ Mm}^{-1}$ between a *lfff* model and the observed filament, we keep the same value for all the following extrapolations. This value corresponds to a normalized value of $\alpha = 0.99$, which is above the critical value above which an OX twisted flux tube is present.

We suppose that the dense absorbing plasma fills a dip up to a depth D which is equal to the pressure scale height H_g . For typical physical values in a prominence, $200 \text{ km} \lesssim H_g \lesssim 500 \text{ km}$. Consequently, in the figures we only represent the dipped portion of field lines of $D = 300 \text{ km}$, at regular space locations.

The last parameter is the flux of the imposed twisted flux-tube, which is constrained by the factor f . In order to estimate the right value of f , we completed several extrapolations with a typical $\alpha = 0.05 \text{ Mm}^{-1}$ making:

- (i) comparisons of the vertical flux of the observed large-scale bipolar field component (seen on Fig. 1d) with the one replacing it, which is introduced by the theoretical background field (as explained in Sect. 3.5),
- (ii) comparisons of the $H\alpha$ filament observed at 12:14 UT (see Fig. 1a) with the modeled configurations (using the method described in Sect. 4.2).

Satisfactory correlations of the model with the observations were found for $8 \lesssim f \lesssim 12$. Thus we use a typical value of $f = 10$ for all the following extrapolations.

4.2. Comparison between $H\alpha$ dark features and dipped field lines in the filament channel

After modifying the SOHO/MDI magnetogram using the method described in Sect. 3.5, the magnetic field is extrapolated in *lmhs* in a 3-D box with horizontal sizes $L_x = L_y = 125 \text{ Mm} = 172''$. The parameters of the model are listed in Table 2. The magnetic dipoles computed from the *lmhs* extrapolation from the modified magnetogram shown in Fig. 1e are reported in Fig. 1b.

4.2.1. Global shape of the filament

The global shape of the computed filament in Fig. 1b shows a satisfactory correlation with the $H\alpha$ image in Fig. 1a. Firstly, the angle of the magnetic dipoles with the inversion line is in ac-

cordance with the orientation of the observed fine structures. Secondly, the initially straight twisted flux-tube forming the filament body is perturbed by the polarities of the filament channel, and it shows very similar features to the observed body of the filament. It is noteworthy that the filament body is also locally deformed in the vicinity of the strong positive polarity, near the largest foot at the middle. This polarity pushes the twisted flux-tube to the left, so that the filament seems to avoid this polarity, in accordance with the observations of Martin et al. (1994) and with the model of Priest et al. (1996).

4.2.2. The lateral feet

The largest foot observed on the right side of the filament (F1) is formed by two main negative parasitic polarities (seen in Figs. 1d,e). The one closest to the filament (N1) forms a broad lateral extension of the dip pattern from the twisted flux-tube, and the other one (N2) creates another set of dipoles which forms a nearly continuous pattern with the first one. Some field lines present two dipoles, in each of these regions. Consequently pressure-driven mass flows along the field lines can easily occur between the broad part of the foot related to N1, which is closer to the filament body, and the thin part related to N2, which is further away from it. It is clear from Fig. 1b that this dip pattern shows a slight interruption between the two parasitic polarities, while this does not appear in $H\alpha$ (see Fig. 1a). Though we believe that this is a minor difference that may be due to some of the reasons given in Appendix B.

Another large lateral foot is observed in $H\alpha$ at the top of the left side of the filament (F2). However the model does only poorly recover this foot from the dipoles distribution (compare Fig. 1a and Fig. 1b). A group of very low lying (below 3 Mm) dipoles are present above a weak positive parasitic polarity, though it does not form a continuous pattern with the filament. This can be due to some of the reasons given in Appendix B.

4.2.3. The chromospheric fine structures

Some dipoles appear away from the filament and its feet in the filament channel (see Fig. 1b). These are also created by parasitic polarities, which are too far from the twisted flux-tube to form a continuous dip pattern with it as in the case of feet. These dipoles are located very low in the atmosphere (below 4 Mm). Such typical isolated and low-lying dipoles have already been associated with observed dark $H\alpha$ fibrils in Paper II and in Aulanier et al. (1998b). In this study, some of them show a correlation with some dark elongated fine structures observed in $H\alpha$ (Fig. 1a): For example, the dark half-circle at the left bottom of the filament (S1), the other one, higher on the left side between the two largest feet (S2), a dark feature located on the right side, oppositely to the upper large foot (S3), and the ‘‘M-shaped’’ group of fibrils on the left of the filament (S4). However, overlaying Fig. 1a and Fig. 1b reveals that this correlation is not as clear as for the filament itself, even if the orientation and location of some of the observed fine structures are well matched by some

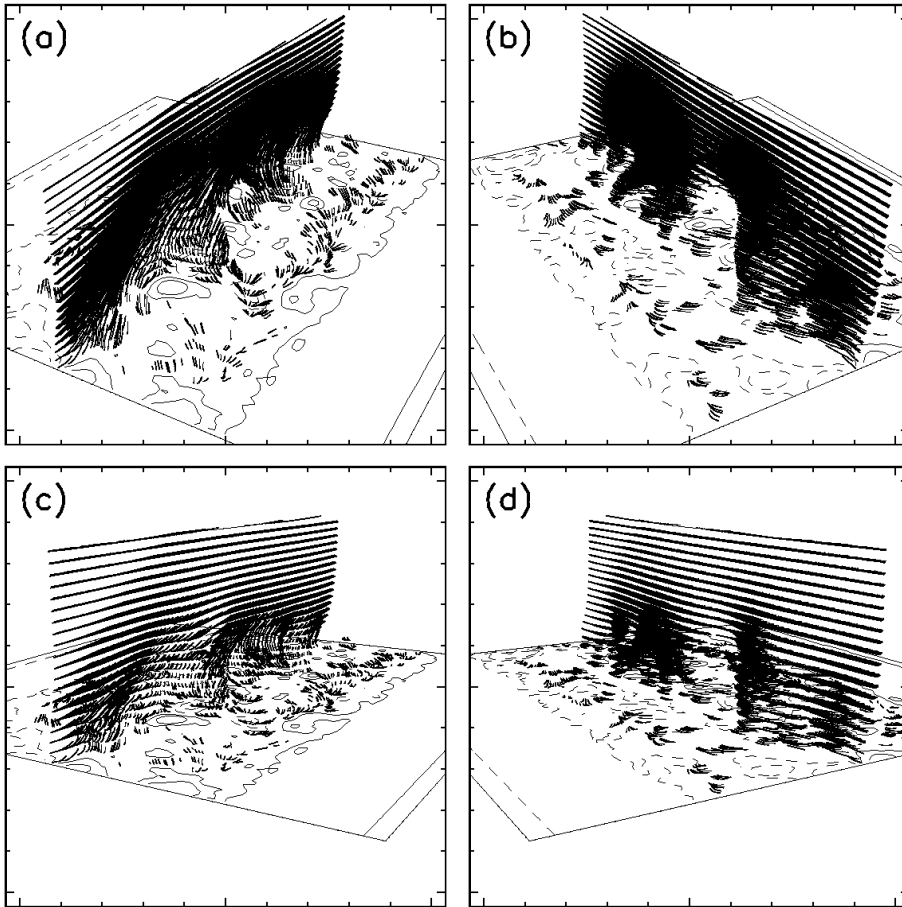


Fig. 2a–d. Side-views of the 3-D *lmhs* prominence model (which is viewed from the top in Fig. 1b). The dark lines correspond to the dips, which are represented up to a depth of $D = 300$ km. The dips are computed at regular intervals: $\Delta x = 0.75$ Mm, $\Delta y = 1.5$ Mm and $\Delta z = 2$ Mm. The thin full (resp. dashed) lines in the photospheric plane correspond to isocontours of the vertical magnetic field of 8 and 24 G (resp. negative values). Note in **a** that some dipped field lines are apparently vertical in the feet due to projection effects. This happens when the magnetic dips are nearly oriented along the line-of-sight.

dip patterns. These differences are probably due to some reasons given in Appendix B.

The orientation of the computed magnetic field in the filament channel is globally parallel to the photospheric inversion line. On both sides of the filament (around $x \simeq \pm 25$ Mm), it shows a typical fishbone structure discovered in $H\alpha$ fibrils by Filippov (1994). This global organization is characteristic of a twisted flux tube located in a bipolar region.

4.3. The filament as a prominence

Fig. 2 shows four different projection views of the computed dips which are viewed from above on Fig. 1b. These projections permit to see the filament as it would be observed near the limb.

The computed prominence is composed by a continuous dipped field line pattern. For viewing purpose the dips are only shown at fixed intervals ($\Delta z = 2$ Mm), leading to the horizontal structures seen on Fig. 2. Reducing the imposed vertical interval between the computed dips would lead to a dark continuous feature, which would not show these horizontal structures anymore, but which would not give a general idea of its 3-D geometry. It is noteworthy in Fig. 2a–d that some very dark regions still appear in the prominence, of which shape and location strongly depend on the projection views. These dark areas are due to the projection effects on the shape of the computed dips. We propose that such variation of the geometrical length along the

line-of-sight affects the measurements of the line-of-sight integrated densities in filaments and prominences using radiative transfer models.

The computed feet (on Fig. 2) are in good qualitative agreement with typical observed feet of prominences and filaments which are close to the limb (e.g. Zirin 1988 pages 267, 268 and Martin, 1990). It is clear from Fig. 2b,c that the series of dips in the largest lateral feet reach the photosphere, forming bald patches (i.e. field lines tangent to the photosphere). The results of Paper II are confirmed here: the feet are not formed by magnetic arcades, but rather by dipped field lines which form a continuous pattern from the prominence body to the photosphere. In this context the magnetic field in the feet is nearly horizontal. Though Fig. 2a shows that projection effects can lead dipped field lines to be apparently nearly vertical in the lower parts of the prominence (e.g. in the foot F1). This happens when the orientation of the magnetic dips is nearly parallel to the line-of-sight. Such false conclusion of nearly vertical structures can also be derived in interpreting observations, where the observed fine structures and the mass flows are projected on the observing plane.

5. The influence of the plasma effects

The effects of pressure and gravity were not included in the previous work presented in Paper II, though the results were

globally satisfactory. We now carry out a linear force-free field (*lfff*) extrapolation of the magnetic field (i.e. $F(z) = 0$) in the filament channel of the modified magnetogram, keeping constant all the parameters of the model (see Table 2), except a which is reduced to zero, to satisfy the *lfff* equations. The aim of this *lfff* extrapolation is to investigate up to what level the plasma effects are important for the magnetic configurations.

5.1. Comparison between *lfff* and *lmhs* extrapolations

The modeled *lfff* filament is represented on Fig. 1c. It can be compared to the *lmhs* filament (see Fig. 1b) and to the observed $H\alpha$ filament (see Fig. 1a). Without plasma effects, the distribution of dips in the body of the filament, the deformation of the twisted flux-tube, as well as the two components for the large foot (F1) are very close to the *lmhs* configuration. However, the angle between the field lines and the photospheric inversion line are much smaller in the *lfff* case. Such small angles are neither consistent with the observed $H\alpha$ fine structures in the body of our filament at 12:14 UT, nor with typical Hanle effect measurements of the magnetic field inside prominences (e.g. Bommier & Leroy, 1998 and references therein).

The effects of pressure and gravity are more important in the case of the isolated dips located in the filament channel. The *lfff* extrapolation only shows very small and dispersed features associated with dipped field lines, while these are much larger in the *lmhs* case (compare Fig. 1c and Fig. 1b). Moreover, some of the isolated dips which appear in *lmhs* are not present at all in *lfff*. As a consequence, there are less observed dark $H\alpha$ features that can be correlated with computed dips in *lfff* than in *lmhs*.

5.2. The importance of pressure and gravity

From this comparison between *lfff* and *lmhs* extrapolations, it can be finally concluded that the influence of pressure and gravity is of secondary importance with respect to the purely magnetic field configuration (in accordance with the conclusions of Aulanier et al., 1998b). However it is noteworthy that the plasma effects are still important in the sense that they slightly modify the magnetic configuration, leading to a better match with observations.

6. Evolution of chromospheric fine structures

We observed the evolution of the quiescent filament channel during 10 hours on September 25th 1996, so that it is possible to investigate the evolution of the 3-D distribution of the dipped field lines. We correlate horizontal motions as well as some emergence of magnetic polarities with the displacement of the feet and the evolution of the $H\alpha$ fine structures.

6.1. Quasi-static evolution

At a first sight, it may appear irrelevant to use the reconstruction of magnetic configurations which are in equilibrium to model an evolution. However, as long as it does not enter an eruptive

phase, the filament evolution is mainly driven by the motions of photospheric magnetic fields. These polarities move with a typical speed of 0.1 to 1 km s⁻¹, which is very small compared to the Alfvén velocity in the corona (of the order of thousands of km s⁻¹) and even in prominences (a few hundreds km s⁻¹). Consequently, the global magnetic field is likely to evolve quasi-statically, hypothesis well justified by the observed velocities (see Sect. 7).

The twisted flux-tube which defines the main body of the filament is not expected to evolve significantly, since this part of the filament was quiescent long before and after the day of September 25th. Moreover, the flux and the horizontal extension of the observed inhomogeneous bipolar background field in the magnetograms do not change significantly during this day. Consequently, the parameters $\tilde{B}(1; 0)$, $\tilde{B}(2; 0)$, $\tilde{B}(3; 0)$, f , L_x , L_y and α can be kept constant. From the observations we have no direct way to estimate the evolution of the plasma parameters a and H so we kept them constant. Using this conservative approach we can miss some evolution in the model, but it has the advantage that the computed dip evolution is only based on a clear observational ground: the evolution of the photospheric magnetic polarities.

6.2. Evolution of the filament channel on September 25th

In this section we extrapolate the magnetic field from modified SOHO/MDI magnetograms. We compare the 3-D distribution of dipped field lines with $H\alpha$ dark features observed with the MSDP. The observing times are given in Table 1. The results are presented on Fig. 3a–h. All the fields of view are 125 Mm \times 125 Mm, or 172'' \times 172''. Then we describe the evolving morphologies of several features. We will always refer to the time of the MSDP ($H\alpha$ images).

6.2.1. The main body of the filament

The straight body of the filament moves away from the strong positive magnetic polarity which is present close to the photospheric inversion line, in the vicinity of N1 and N2 (see Sect. 4.2.2). It has the same polarity as the background field on the right-hand side of the inversion line (i.e. positive polarity). As this polarity decreases in flux and moves away from the main inversion line (see Fig. 4), the global distribution of dips becomes more straight along the inversion line as does the filament body in $H\alpha$ from 08:43 UT to 17:04 UT (see Fig. 3). However, one cannot strictly associate the changes to only one polarity, they are also partly due to the evolution of the neighboring polarities.

On the other hand, where there is a parasitic polarity, the twisted flux-tube as well as the low-altitude portions of neighboring field lines are locally bent towards the photosphere, forming new dips (e.g. the group of positive polarities at the top-left side of the filament in Fig. 3a,b). The evolution of these polarities close to the photospheric inversion line is closely related to the changing of the shape of the filament body.

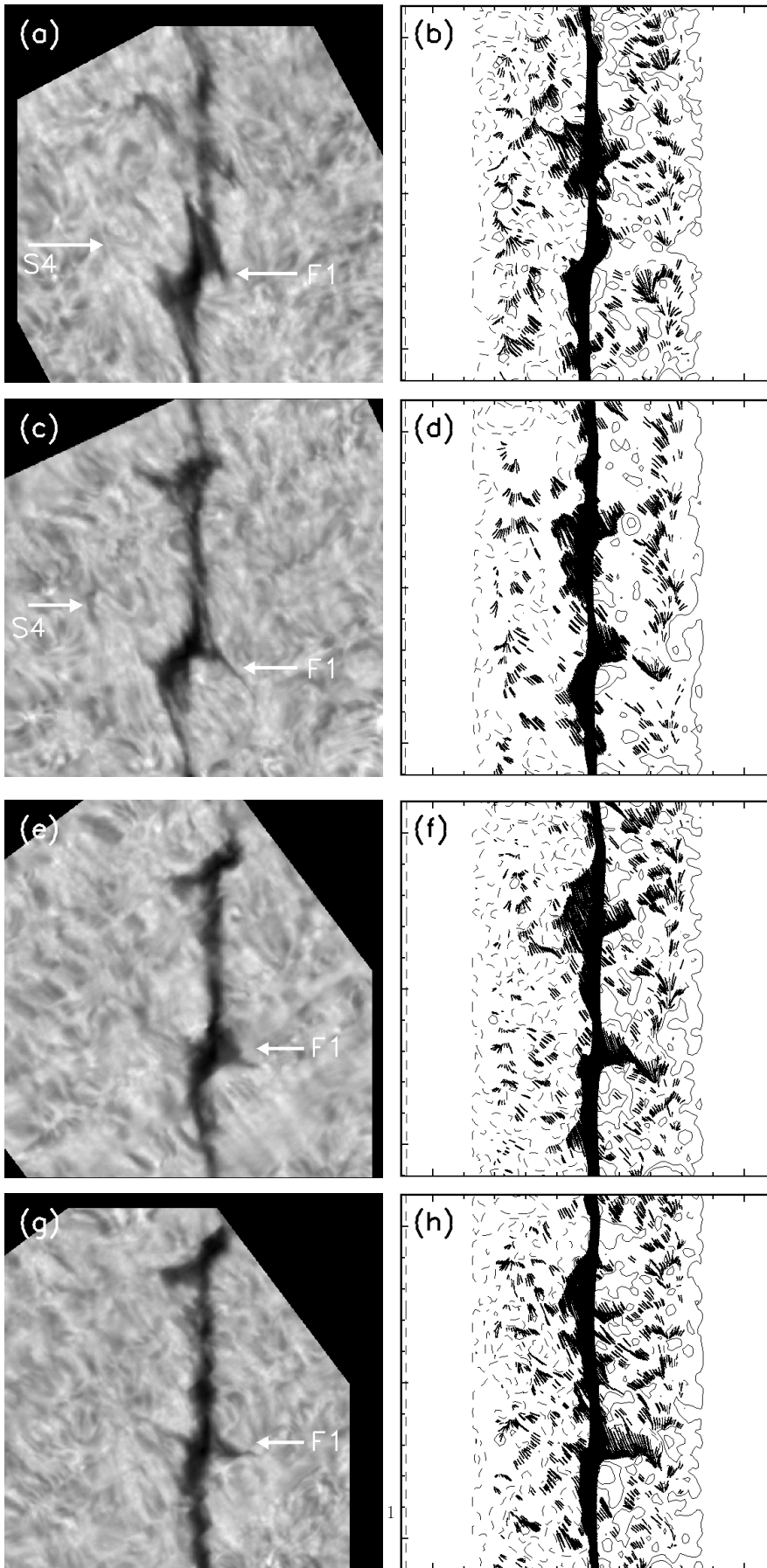


Fig. 3a–h. Evolution of the filament channel on September 25th 1996. **a, c, e** and **g** show the filament channel observed with the MSDP in $H\alpha$ at 08:43 UT, 12:14 UT, 15:57 UT and 17:04 UT respectively. **b, d, f** and **h** show the 3-D distribution of the dipped field lines computed in *lmhs* (using the parameters given in Table 2) from the modified SOHO/MDI magnetogram obtained at 07:40 UT, 12:53 UT, 15:59 UT and 17:35 UT, respectively. The drawing convention is the same as in Fig. 1b,c.

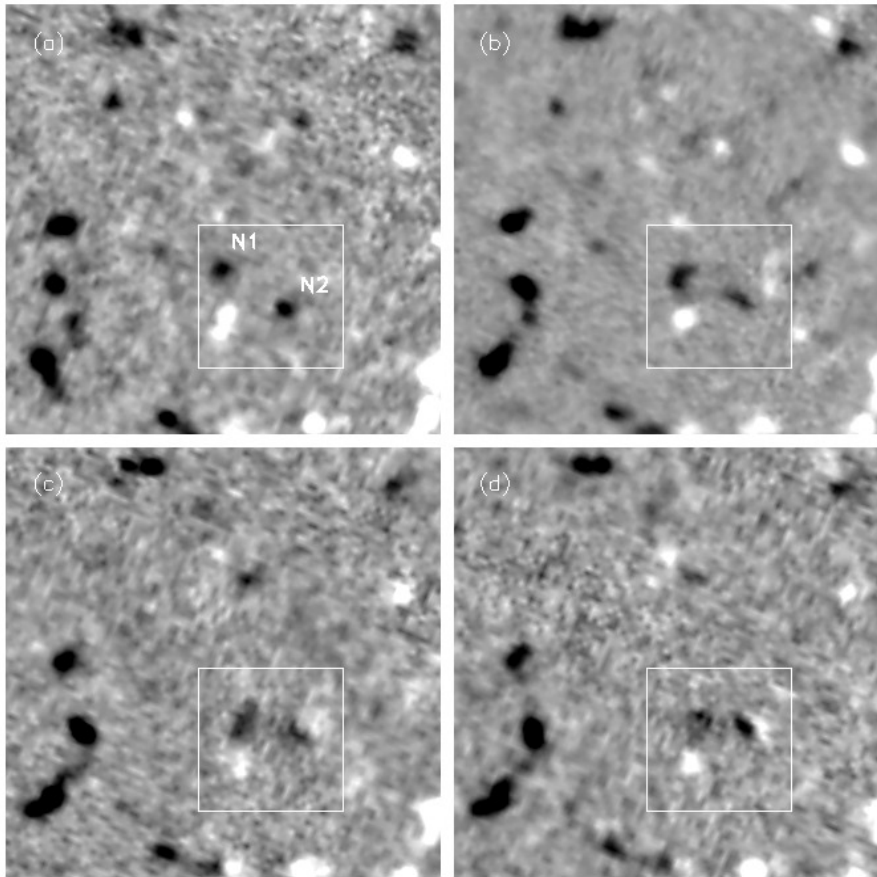


Fig. 4a–d. Co-aligned magnetograms of the filament channel on September 25th 1996. **b–d** show the filament channel observed with SOHO/MDI at 07:40 UT, 12:53 UT, 15:59 UT and 17:35 UT, respectively. The box highlights the evolution of the parasitic polarities in the vicinity of the filament foot F1. Note the change in the position and strength of N1 and N2.

6.2.2. Correlation between the feet and the parasitic polarities

In this evolution, the best modeled foot is the largest one which is at the middle-right of the filament (F1). At 08:43 UT, F1 is not well formed (see Fig. 3a,b). The two negative polarities which form it are far from one another (see Fig. 4a): N1, which is very close to the inversion line (only leading to a weak perturbation of the filament body), and the other one N2, is at approximately 20 Mm on the right (it forms an isolated dip pattern). By 12:14 UT, both polarities have moved towards each other (see Fig. 4b), leading to a large and quasi-continuous dip pattern which forms the lateral foot F1 (see Fig. 3c,d). From 15:57 UT to 17:04 UT the polarity N2 gradually moves to the north (see Fig. 4c,d). This leads to a displacement of F1 which gets more and more perpendicular to the filament (Fig. 3e–h).

Some other large and dark lateral extensions appear at different times, which have the characteristics of lateral feet. A careful look at them reveals that, even if they are not as well modeled as the foot F1, their observed main shape and evolution in $H\alpha$ are recovered from the *lmhs* extrapolations (see Fig. 3). From this study the location and evolution of the lateral feet can now be correlated to those of parasitic polarities.

6.2.3. The evolution of the “M-shaped” fine structure

We leave to the reader a detailed comparison between all the observed dark features with the distribution of dipoles (as there

are many to look at, and as we do not want to describe all these in details), taking into account the problems expressed in Appendix B.

We only describe below the evolution of one of the groups of dark fibrils which is well observed and fairly well modeled. This dark feature was previously named as S4 in Fig. 1a,b at 12:14 UT. It shows an “M-shaped” dark pattern at 08:43 UT (see Fig. 3a and the Box 4 in Fig. 5). S4 is formed by a group of weak parasitic polarities. Their maximum vertical field is approximately equal to 10 G at 08:43 UT, and they form a set of very low lying dipoles which appear below 2 Mm (see Fig. 2b,d). The dip pattern of S4 is not continuous, so it is not easy to recognize the M-shape, though a careful look at the orientation and location of the computed dipoles shows an agreement with the observed “M-shaped” structure in $H\alpha$. The $H\alpha$ feature S4 evolves with time, and it is slightly shifted upwards of the represented field of view by 12:14 UT (Fig. 3c). For the later observing times, the magnetic flux of the corresponding polarities is more dispersed, though they still form some new isolated dipoles. This “M-shaped” fine structure is replaced by a set of $H\alpha$ fibrils nearly parallel to the filament. The computed dipoles follow this trend (see Figs. 3e–h).

7. Dopplergrams of $H\alpha$ dark features

In this section the link between some observed $H\alpha$ dark features and their associated observed Dopplershifts is investigated. In

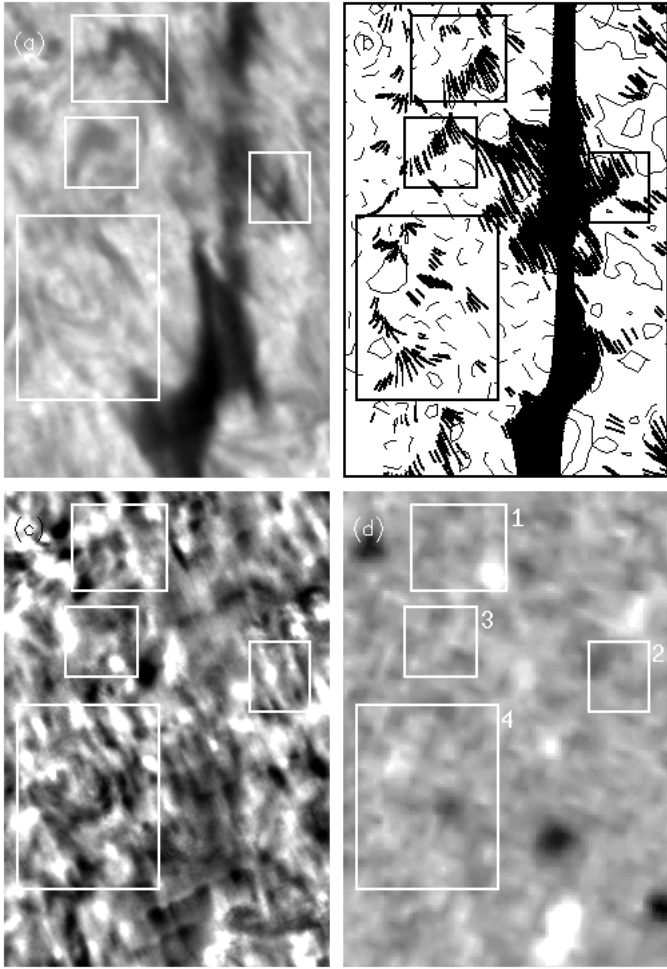


Fig. 5. **a** is a zoom on the filament channel observed in $H\alpha$ with the MSDP at 08:43 UT. **b** is the corresponding field of view of the model taken from Fig. 3b. **c** shows the $H\alpha$ Dopplergram deduced from the MSDP data at 08:43 UT. Black (resp. white) refers to blueshifts (resp. redshifts). Dopplershifts are derived by the line bisector method at $H\alpha \pm 0.25 \text{ \AA}$. **d** shows the co-aligned SOHO/MDI magnetogram obtained at 07:40 UT. The field of views are $106 \text{ Mm} \times 73 \text{ Mm}$ or $147'' \times 100''$.

order to do so we present a zoomed portion of the filament channel observed at 08:43 UT (Fig. 5).

7.1. Method for measuring dopplershifts

The Doppler velocities presented in Fig. 5c have been calculated by using the method of line-bisector at $\pm 0.25 \text{ \AA}$ from line center. They correspond to line-of-sight velocities only in the case of optically thick structures. For typical chromospheric fine structures, the expected underestimation factor is between 1 and 4 (Alissandrakis et al., 1990). Radiative transfer calculations using “cloud models” are necessary to convert dopplershifts into accurate velocities.

The zero-value of dopplershifts is determined by averaging the data over the whole field of view. Blueshifts of filaments are included as well as redshifts of network cell boundaries, so that the accuracy of the result is probably not better than a

Table 3. Average Doppler velocities measured in the dark $H\alpha$ fine structures which are located in the four Boxes defined on Fig. 5.

v_z (km s^{-1})	Box 1	Box 2	Box 3	Box 4
average	+0.0	+0.1	+0.2	+0.6

few hundreds of m s^{-1} . However, relative dopplershifts between neighbouring points are determined more accurately.

The minimum and maximum dopplershifts in the field of view are $\pm 7 \text{ km s}^{-1}$. The filament body shows typical weak upward motions from few hundred m s^{-1} up to 3 km s^{-1} , in accordance with several previous studies (e.g. Schmieder, 1990 and Mein et al., 1994).

7.2. Description of fine structures

Four boxes are defined on Fig. 5a-d, which enclose the fine structures discussed in the following. Box 1 shows the forming top-left foot F2 of the filament, Box 2 shows a small lateral foot on the right of the filament which disappears later, Box 3 shows an elongated and curved fine structure, and Box 4 shows S4 (as defined in Fig. 1a) which is the “M-shaped” group of fibrils discussed in Sect. 6.2.3.

Comparing Fig. 5b and Fig. 5d confirms that the lateral dip structures are created by parasitic magnetic polarities, i.e. positive ones for Boxes 1,3,4, and negative ones for Box 2. Comparing the shape of the $H\alpha$ features (in Fig. 5a) with the distribution of dipoles (in Fig. 5b), it is noteworthy that the orientation of the fine structures do not necessarily correspond to the orientation of their inner magnetic field. For example, looking at Box 3 clearly shows that \mathbf{B} is perpendicular to the elongated fine structure, and that this elongated shape is mainly due to the continuous dipoles pattern.

7.3. Vertical motions in the fine structures

The observed filament was nearly at the disc center on September 25th (S2, E5), consequently the Doppler velocities nearly correspond to the vertical velocities v_z of the plasma.

Let us focus on the four boxes. A first look at Fig. 5c shows that their associated $H\alpha$ dark fine structures mainly present low upward velocities (compare Figs. 5a,c). By averaging typical dopplershifts taken at 20 points along each structure, we obtain the values listed in Table 3.

The observed velocities in the fine structures are much closer to the driving velocities of photospheric magnetic polarities ($0.1 \text{ km s}^{-1} < v(\text{phot}) < 1 \text{ km s}^{-1}$) than to the typical magnetic velocities (i.e. Alfvén velocity), in spite of their possible underestimation due to their small optical thickness (see discussion in Sect. 7.1). This has the following natural explanation. The slow horizontal motions of parasitic polarities are expected to cause a global quasi-static evolution of the 3-D magnetic configuration: the magnetic field lines are progressively deformed so that the dipoles are horizontally and vertically displaced. Because the ion-

isation is sufficient to freeze the plasma in the magnetic field, we propose here that the Dopplershifts represent these vertical motions. The observed motions are in accordance with the support of the plasma in magnetic dips (in the vertical direction the tension term of the Lorentz force nearly balances the gravity, plasma and magnetic pressure forces). Along the magnetic field, so in a nearly horizontal direction, plasma flows can be driven, for example by pressure differences. Observations show typically higher horizontal velocities than vertical ones by a factor 10. (e.g. see Schmieder, 1990). Such horizontal velocities can be at the origin of a shift between the observed $H\alpha$ dark material and the computed dips. The present results put a constraint on this effect.

8. Conclusions

We have performed a detailed comparison of $H\alpha$ observations with the 3-D model for the magnetic configuration supporting quiescent filaments developed in Papers I and II. The model is based on the initial simple idea that filaments are formed by cold plasma trapped in magnetic dips. The main aim was to develop a model which could be compared precisely to observations and which could reproduce the feet of prominences, which have been a long-standing puzzle.

In the present paper we have extended the comparison to observations which we started in Paper II, using a series of SOHO/MDI line-of-sight magnetograms, as well as high resolution $H\alpha$ spectro-imaging data taken with the MSDP instrument on the German VTT (Tenerife). These observations were obtained during a coordinated campaign between space instruments aboard SOHO, Yohkoh and ground-based instruments, on September 25th 1996. In order to model the magnetic field in the observed filament channel, we used the linear magneto-hydrostatic (*lmhs*) extrapolation method developed by Low (1992). This method extends the usual linear force-free field (*lfff*) extrapolation by including the effects of plasma pressure and gravity. The present study is the first attempt to use *lmhs* extrapolations in an observed filament channel. The inputs to the model are the observed photospheric longitudinal magnetic field (which was modeled by magnetic charges in Paper II), as well as a few parameters (see Table 2) which are estimated from the observations. The observed velocities of the photospheric magnetic polarities and of the plasma in the filament justify the present quasi-static approach used to study the filament evolution. The main hypotheses remain on the implicitly supposed distribution of the electric currents and the presence of a twisted flux-tube in the corona. These limitations are presently inherent not only in observations (in particular the absence of vector magnetograms), but also in the present modelling (due to difficulties to build 3-D non-linear models with observable boundary conditions).

Using the above assumptions (and keeping in mind the limitations given in Appendix B) the localization of the dips are in a surprisingly good agreement with the $H\alpha$ fine structures, both in the filament (body and feet) and in its channel (dark elongated fibrils). This finally justifies the chosen approach. The

comparison of the model with $H\alpha$ observations is done through the computation of the field lines limited to their magnetic dips, filled up to a depth of 300 km (typical gravitational scale height of the plasma in filaments). In this way the *lfff* extrapolations give a fairly good localization of the filament body and feet. Including plasma pressure and gravity via *lmhs* extrapolations slightly improves the correlation with $H\alpha$ fine structures. It extends the distribution of dips and rotates the field direction towards the orientation of the observed $H\alpha$ fine structures. While we have forced the model to over-estimate the plasma effects up to the limit of physical validity, we still found that the plasma effects only lead to a relatively small deformation of the magnetic configuration. The locations of dips are mainly constrained by the magnetic shear and by the photospheric field distribution. It is also noteworthy that the exact distribution of the coronal electric currents is not of such a great importance (though it is more important than the plasma distribution) provided that a main twisted flux-tube is present together with the parasitic polarities.

In the filament channel $H\alpha$ dark features are usually present in the vicinity of low measured vertical magnetic fields at the limit of the instrumental noise of SOHO/MDI ($B_z \simeq 10$ G). Nevertheless, some of the $H\alpha$ dark features can be correlated with low lying computed dipped field lines ($z < 2$ Mm). Consequently, despite of many of the theoretical and observational problems listed in Appendix B, the detailed comparison of the model with the observations can still be completed under such extreme conditions. This is in agreement with the results obtained by Aulanier et al. (1998b) on $H\alpha$ fibrils in an active region, with data from different instruments.

This series of papers brought further evidences of that twisted configurations are supporting at least some filaments in bipolar regions. The present model is a 3-D extension of previous twisted flux-tube models such as van Ballegoijen & Martens (1989), Démoulin & Priest (1989), Priest et al. (1989) and Low & Hundhausen (1995). The twisted flux-tube concept brings together, in a natural way, many of the so-long unrelated observations (see conclusion of Paper I). It explains the feet as a natural extension of the filament body, composed of a continuous dip pattern which joins the prominence body to the photosphere. These lateral dips form a natural extension of the central distribution of dips (in the prominence body), due to the presence of parasitic polarities in the filament channel. The shape and the evolution of the feet are linked to these observed parasitic polarities. The 3-D aspect of the model permits to make the link between the organization of the dips viewed from above (filaments) and from the side (filaments close to the limb and prominences).

Comparisons between filament/prominence models and observations bring new information on the highly non-potential magnetic configurations of the solar atmosphere. In a more general context, such investigations link the studies of the rise of magnetic flux-tubes through the convection zone to the CMEs in the corona and their associated interplanetary magnetic clouds. We hope that all the points emphasized in this paper will provide some insight so that observers and theoreticians can collaborate

in order to apply relevant 3-D models of filaments/prominences through well oriented observing programs. In this context we hope to use the future observations from the French-Italian telescope THEMIS based at the Teide Observatory (Tenerife), which should provide simultaneous high cadence spectro-imagery and magnetic data.

Appendix A: physical justification for the twisted flux-tube

The inclusion of an artificial background magnetic field creating a twisted flux-tube in the observed fields in the filament channel can be questioned. The main reason is that it modifies the observed magnetograms (e.g. see the difference between Fig. 1d and Fig. 1e). However, there are several arguments that justify this method.

(i) From Paper I: A systematic study of all the *lfff* configurations using the $(\tilde{B}_2; \tilde{B}_3)$ diagrams for different values of α has revealed that the OF twisted flux tube was the best configuration satisfying many different observational aspects of filaments and prominences, in particular the Hanle effect measurements of the magnetic field inside prominences, as well as underlying feet, lateral feet and chirality patterns of filaments. This “OF” terminology refers to an O-point at the center of the twisted flux tube and a flat field line at its bottom, with two X-points on the side (see Paper I).

(ii) From Paper II: OF twisted flux-tubes have been proven to be equivalent to OX flux-tubes perturbed by parasitic polarities in their vicinity, and the detailed study of the morphology of the lateral dipped structures associated with theoretical and observed parasitic polarities gave satisfactory results.

(iii) The presence of twisted configurations which support filaments could be a natural consequence of their build-up in the convection zone. Emonet & Moreno-Insertis (1998, and references therein) have shown that a minimum critical twist is needed so that a buoyant 2.5-D flux-tube is not destroyed during its rise by the hydrodynamic wakes which develop behind it. Moreover, for twists which are higher than the critical one, the combination of a higher buoyancy force in the central part of the flux-tube with the effect of the following wakes deform the magnetic configuration to the typical OF configuration. These results have been confirmed by Fan et al. (1998). The magnetic topology found in these MHD simulations is basically the same as the one found in *lfff* in Paper I which was there proven to be reliable for typical filaments. So far the MHD simulations studied the deep convection zone and not the emergence of the flux-tube through the photosphere, but it is very tempting to link these results. It is not yet fully clear how the dense plasma contained in the rising flux-tube is released through this emergence but it is thought to be a difficult and long process (see e.g. Low 1996), which is compatible with the long life of filament channels.

(iv) The prominence twisted flux-tube is also in agreement with the topology inferred from CMEs observed with the SOHO/LASCO coronagraph (e.g. Chen et al. 1997). In the interplanetary medium, twisted configurations are also identified in magnetic clouds (or interplanetary CMEs) with in situ mea-

surements from Ulysses (e.g. Bothmer et al., 1996 and Weiss et al., 1996). The link between CMEs and prominence eruptions is highly probable both on a statistical ground (e.g. Bothmer & Schewnn 1994) and on deep study of individual cases (e.g. Burlaga et al., 1998).

(v) No twisted flux-tube can be found from direct *lfff* or *lmhs* extrapolations of the magnetograms. However, this is not inconsistent with the presence of such a flux-tube in the filament channel: a twisted flux-tube could be created by concentrated currents, which would not modify the vertical distribution of the magnetic field B_z in the observed fields. Modelling such a magnetic configuration would require 3-D non-linear extrapolations in *nlfff* or *nlmhs* (e.g. Sakurai, 1989). Their effect would only be visible on the observed horizontal fields. Unfortunately, no measurements of the transverse fields are available for such low-field regions as filament channels, so that no observational constraint can be put on these currents. In this study we keep a “linear” approach (as in Papers I and II).

Appendix B: how can we explain the minor differences between the model and the observations?

In Sects. 4.2 and 6.2, we showed that the location, shape and orientation of most of the dark H α absorbing features are correlated with the 3-D distribution of dipped field lines. However, some of these observed fine structures were poorly modeled by magnetic dips. We enumerate here all the reasons which we believe that may be the cause of these minor discrepancies, starting from the most probable ones and finishing with the less likely ones:

(i) Inhomogeneities of the shear distribution can be present. Their full treatment would require *nlmhs* extrapolations for which $\alpha \neq$ constant. Moreover, we cannot determine precisely the flux-tube parameters from the present observations. In order to do so, we would need transverse field measurements.

(ii) Some parasitic polarities observed by SOHO/MDI (see Fig. 1d) are very weak and may not always be reliable: their vertical field is below 10 G, which is very close to the instrumental noise of MDI (see Sect. 2.2 for details).

(iii) Every magnetic dips are not necessarily filled by dense and cold plasma, since this is determined by the energy balance of the plasma.

(iv) The function $F(z)$ used is only a crude treatment of pressure and gravity in the filament channel. Other functions $F(z)$ could be used, but a significant progress would require the description of the important density contrast between the prominence and the corona.

(v) The model does not take into account the effects of radiative transfer. In particular, the visibility of the fine structures is expected to be low where the density variations in the dips are not large compared to the chromospheric density.

(vi) Some parasitic polarities are weakly modified by the introduction of the background field of the twisted flux-tube (compare grey levels between Fig. 1d and Fig. 1e).

(vii) The magnetic polarities have probably evolved between the observing time in $H\alpha$ and the one of the magnetogram (see Table 1).

(viii) The periodicities of the model in the x and y directions introduce an artificial deformation of the configuration at the border of the computational box. In particular in the x direction, perpendicularly to the filament axis, the effect of the periodic boundary conditions in the main bipolar background photospheric field is to reduce the area in which field lines can connect these two opposite polarities (forming arcades overlaying the imposed twisted flux tube), compared to an extrapolation method which would not impose such periodicities. Consequently the field line connectivity is poorly modeled in these regions for $x \geq \pm 37$ Mm, and the present method models the filament channel as if the observed inhomogeneous bipolar component was in fact less than 125 Mm wide, which is the period of the imposed boundary conditions.

(ix) Pressure-driven flows of dense plasma along flat field lines, can be observed in the $H\alpha$ line center as horizontal flows. However, as this moving plasma is not located in magnetic dips, our representation cannot show it.

Acknowledgements. The authors thank J.-M. Malherbe, C. Coutard, R. Hellier, J. Staiger and the German team of the VTT for their active participation in the MSDP observations, as well as L. Harra-Murnion for her comments on the manuscript. LvDG acknowledges the research grant OTKA T026165. Our ground-based campaign had received observing time under the International Time Program offered by the CCI of the Canarian Observatories and supported by the European Commission through the Access to Large Facility “Activity of the Human Capital and Mobility Program”. It was also supported by the INSU and the GdR of CNRS “Magnétisme dans les étoiles de type solaire”. The authors thank the SOHO/MDI consortium for the magnetograms, courtesy of C. DeForest. This research was carried out in the framework of the SOHO Guest Investigator program (1998/1999). SOHO is a project of international cooperation between ESA and NASA.

References

- Alissandrakis C.E., Tsiropoula G., Mein P., 1990, A&A 230, 200
 Antiochos S.K., Dahlburg R.B., Klimchuck J.A. 1994, ApJ 420, L41
 Aulanier G., Démoulin P., 1998, A&A 329, 1125 (Paper I)
 Aulanier G., Démoulin P., van Driel-Gesztelyi L., Mein P., DeForest C., 1998, A&A 335, 309 (Paper II)
 Aulanier G., Démoulin P., Schmieder B., Fang C., Tang Y.H., 1999, Solar Phys. submitted
 Berger, M.A., 1998, In: Webb D., Schmieder B., Rust D. (eds.) IAU Colloq. 167, ASP conference series, 102
 Bommier V., Leroy J.L., 1998, In: Webb D., Schmieder B., Rust D. (eds.) IAU Colloq. 167, ASP conference series, 434
 Bothmer V., Schwenn R. 1994, Space Sci. Rev. 70, 215
 Bothmer V., Desai M.I., Marsden R.G., Sanderson T.R., Trattner K.J., et al., 1996, A&A 316, 493
 Burlaga L., Fitzenreiter, Lepping R., et al., 1998, JGR 103, A1, 277
 Démoulin P., 1998, In: Webb D., Schmieder B., Rust D. (eds.) IAU Colloq. 167, ASP conference series, 78
 Démoulin, P., Priest, E.R. 1989, A&A 214, 360
 Démoulin P., Bagalá L.G., Mandrini C.H., Hénoux J.C., Rovira M.G. 1997, A&A 325, 305
 Emonet T., Moreno-Insertis F., 1998, ApJ 492, 804
 Fan Y., Zweibel E.G., Lantz S.R., 1998, ApJ 493, 480
 Filippov B.P., 1994, Astron. Letters 20, 665
 Kuperus M., Raadu M.A. 1974, A&A 31, 189
 Low B.C., 1991, ApJ 370, 427
 Low B.C., 1992, ApJ 399, 300
 Low B.C., 1996, Solar Phys. 167, 217
 Low B.C., Hundhausen J.R., 1995, ApJ 443, 818
 Martin S.F., 1990, In: Ruždjak V., Tandberg-Hanssen E. (eds.) IAU Colloq. 117, 1
 Martin S.F., Bilimoria R., Tracadas P.W., 1994, In: Rutten R., Schrijvers C. (eds.), Solar Surface Magnetism. Kluwer Ac. Pub., 303
 Mein P., 1991, A&A 248, 669
 Mein N., Mein P., Wiik J.E., 1994, Solar Phys. 151, 75
 Priest E.R., Hood A.W., Anzer U., 1989, ApJ 344, 1010
 Priest E.R., van Ballegooijen A.A., Mackay D.H., 1996, ApJ 460, 530
 Sakurai, T., 1989, Space Sci. Rev. 51, 11
 Scherrer P.H., Bogart R.S., Bush R.I., et al., 1995, Solar Phys. 162, 129
 Schmieder B., 1990, In: Ruždjak V., Tandberg-Hanssen E. (eds.) IAU Colloq. 117, 85
 Schmieder B., Démoulin P., Aulanier G., Golub L., 1996, ApJ 467, 881
 van Ballegooijen A.A., Martens P.C.H., 1989, ApJ 343, 971
 Weiss L.A., Gosling J.T., Mc Allister A.H., et al., 1996, A&A 316, 384
 Zirin H., 1988, Astrophysics of the Sun, Cambridge University Press